Journal of Non-Crystalline Solids 500 (2018) 133–140

Contents lists available at ScienceDirect

Journal of Non-Crystalline Solids

journal homepage: www.elsevier.com/locate/jnoncrysol

Synthesis and structural characterization of a new $SbPO_4$-GeO_2 glass system

Murilo Montesso[a,e], Danilo Manzani[b], José P. Donoso[c], Claudio J. Magon[c], Igor D.A. Silva[c], Mario Chiesa[d], Elena Morra[d], Marcelo Nalin[a,*]

[a] Institute of Chemistry, São Paulo State University – UNESP, 14800-060 Araraquara, SP, Brazil
[b] São Carlos Institute of Chemistry, University of São Paulo – USP-IQSC, 13566-590 São Carlos, SP, Brazil
[c] São Carlos Institute of Physics, University of São Paulo -USP-IFSC, 13566-590 São Carlos, SP, Brazil
[d] Dipartimento di Chimica, Università di Torino, Via P. Giuria, 7, 10125 Turin, Italy
[e] Chemistry Department, Federal University of São Carlos, 13565-905 São Carlos, SP, Brazil

ARTICLE INFO

Keywords:
Glass
Antimony phosphate
Germanate
Structure

ABSTRACT

This work presents the production and characterization of a new prolific binary glass system based on $SbPO_4$-GeO_2. The dependence of GeO_2 content on thermal, structural and optical properties were investigated by means of thermal analysis, Raman, UV–Vis-NIR, infrared, M-lines and EPR spectroscopy. Glass transition temperatures remain constant around 410 °C when GeO_2 content is increased, indicating that GeO_4 units are not responsible for increasing the connectivity of PO_4 units. Thermal stability linearly increases as a function of GeO_2 content, reaching a value around 400 °C for glass containing 90 mol% of GeO_2. Raman spectroscopy was used to evaluate the glass structural changes when GeO_2 is incorporated from 30 to 90 mol% indicating a gradual change from a phosphate to a germanate glass skeleton. The optical window extends from 350 nm at UV region, up to 2.7 μm in the middle-infrared region limited by the multiphonon cut-off due to the strong OH absorption. M-lines technique shows that increasing GeO_2 content decreases the refractive index, mainly because the lower concentration of higher polarizable antimony atoms. EPR spectra of heat treated V_2O_5 doped glasses, at different temperatures above the glass transition temperature, shows the characteristic eight-line hyperfine splitting spectrum. The spin Hamiltonian parameters obtained from the simulated spectra indicates that the paramagnetic tetravalent vanadium ions in the glasses exist as vanadyl form VO^{2+}, located in axially distorted octahedral sites. For glasses treated at higher temperatures a second VO^{2+} component appears in the EPR spectra and the analysis of the spin-Hamiltonian parameters suggests that these vanadyl ions are in more tetragonal distorted octahedral sites than those in the glass.

1. Introduction

Nowadays an intense demand is occurring for the development of new glass materials having specific characteristics such as large infrared transparency [1], excellent optical quality [2], high linear (n_0) and nonlinear refractive indices (n_2) [3–4], large rare-earth ions (RE^{3+}) solubility [5] and good chemical durability. These glasses have been extensively used in different fields of photonics and production of devices, such as optical fibers [6], integrated optical circuits [7], optical amplifiers [8] and solid-state lasers [9].

It is well known that antimony-based glasses have the aforementioned features and have been increasingly studied for applications due to their high linear refractive index [10–11], large transmittance window from ultra-violet (350 nm) to near infrared regions (4 μm) [11,12], low glass transition (T_g) and softening temperatures, allowing drawing of these glasses as optical fibers. In addition, germanate based glasses (based on GeO_2) have received much attention due to their unique physical and optical properties, such as high RE^{3+} solubility, excellent chemical durability, and wide infrared transparency up to 4 μm [13]. Germanate glasses present similar phonon energies and infrared transmission cut-off wavelengths compared to tellurite glasses [6,14] and lower than silicate glasses [15]. Nevertheless, germanate glasses exhibit higher glass transition temperatures enhancing their mechanical and thermal stabilities compared with other oxide glasses making them an attractive alternative material for infrared optical fiber applications [14].

In this sense, glasses presenting high transparency from UV to near-IR, with large nonlinearity, high thermal stability, and high linear refractive index are potential candidates to be used in integrated optical devices, optical switches [16], optical amplifiers [17], and infrared

* Corresponding author at: Laboratório de Vidros Especiais – LaViE, Institute of Chemistry, São Paulo State University – UNESP, 14800-060 Araraquara, SP, Brazil.
E-mail address: marcelo.nalin@unesp.br (M. Nalin).

https://doi.org/10.1016/j.jnoncrysol.2018.07.005
Received 21 May 2018; Received in revised form 3 July 2018; Accepted 4 July 2018
Available online 03 August 2018

fibers [14]. Moreover, the combination of physical, rheological, mechanical and optical properties showed by the new germanate-antimony-orthophosphate based glasses turns the investigations of their thermal, structural and optical properties of great interest.

Electron paramagnetic resonance (EPR) spectroscopy is recognized as a powerful tool for the study of local environment of paramagnetic transition metals because it provides information about the valence state, the coordination geometry and the site symmetry of the paramagnetic center [18–20]. In particular, the tetravalent vanadium specie, V^{4+}, has been used as a spectroscopic probe for characterization of solid-state systems because their continuous-wave (CW) EPR spectra have a characteristic eightfold hyperfine structure of the EPR lines [19–21]. Common valence states of vanadium are +2, +3, +4, +5. The +2 and the +3 states, although paramagnetic, are rarely observable by EPR [22]. The +5 (diamagnetic) and the +4 (paramagnetic) are the most frequent valence states of vanadium in oxide glasses [23,24]. In these glasses, the V^{4+} ion appears almost exclusively as a vanadyl form, VO^{2+} [25–27]. EPR has been successfully employed in glass research because the VO^{2+} EPR spectra is easily observable until room temperature and the spin-Hamiltonian parameters, such as the *g*-tensor and the hyperfine coupling *A*-tensor are sensitive to the local environment around a paramagnetic species and the changes in the coordination geometry and ligand binding resulting from, for example, thermal treatments of glasses [28–30]. X-band and Q-band CW EPR spectra of V_2O_5-doped $SbPO_4$ – GeO_2 glasses and samples heat treated at temperatures between glass transition and onset of crystallization were reported here. Hyperfine interactions between the electron spin and remote magnetic nuclei, present in the surroundings of the paramagnetic V^{4+} ion, were investigated by Hyperfine Sublevel Correlation spectroscopy (HYSCORE).

In this work, we present a systematic study of the glass formation of a new binary glass system based on $SbPO_4$-GeO_2, as well as the thermal, optical and structural characterizations by using DSC, Raman, UV–Visible, near-IR transmittance, M-lines and EPR spectroscopy measurements. The insertion of V^{4+} ions as V_2O_5, was used as a paramagnetic structural probe in order to help the evaluation of the structural changes by composition.

2. Experimental

2.1. Glass composition and sample preparation

Glass samples were synthesized by the conventional melt-quenching method by using commercial raw material GeO_2 (Alfa Aesar, 99.999%), and $SbPO_4$ prepared according to Nalin and collaborators [11]. The reagents were stoichiometric weighted and mixed in an agate mortar, then loaded in a Pt/Au crucible for melting. The melting temperatures varied from 1100 to 1200 °C, depending on the GeO_2 content, under environmental atmosphere during 30 min to ensure total homogenization and fining. Glass samples were obtained according to the composition rule (*100-x*) $SbPO_4$- *x* GeO_2 with x = 30, 40, 50, 60, 70, 80 and 90 mol%. Melted batch samples were cast into a stainless-steel mold preheated 20 °C below glass transition temperature (T_g), followed by an annealing at the same temperature for 2 h to reduce thermal stresses. All samples are colorless and transparent. In order to help structural elucidation and evaluate the role of V^{4+} as a paramagnetic structural probe, the sample $60GeO_2$-$40SbPO_4$ (in mol %) was doped with 0.1 mol % of V_2O_5 and sliced in four pieces: one kept as prepared glass, and the others thermally treated at 440, 470 and 500 °C for 1 h in order to induce structural changes in glasses.

2.2. Characterization techniques

Glass transition temperature (T_g), onset of crystallization temperature (T_x), crystallization peak (T_p) and thermal stability parameter ($\Delta T = T_x - T_g$) data were obtained from differential scanning calorimetry (DSC) in the temperature range of 300–800 °C carried out under N_2 atmosphere. Glass pieces of around 20 mg were loaded into a platinum pan and heated at a heating rate of 10 °C.min^{-1}, using a NETZSCH equipment, model DSC 404 F3 Pegasus, with a maximum error of ± 2 °C for T_g and T_x and 1 °C for Tp.

Raman spectra were obtained using polished bulk samples with a Jobin-Yvon Horiba LABRAM-HR-800 micro Raman spectrometer equipped with a He/Ne laser excitation source (632 nm) in the range from 100 to 1400 cm^{-1} and resolution of 1 cm^{-1}.

The optical window was measured from UV to middle infrared region. Optical characterizations were performed on glass bulks with ~2 mm of thickness and having parallel and optically polished faces. Their optical absorption spectra were recorded in the range of 200–2000 nm using a Varian Cary 5000 spectrophotometer. Infrared measurements were carried out from the bulk samples from 2.0 to 5.0 μm using a Perkin Elmer-FTIR 2000 spectrophotometer.

The linear refractive indices were obtained by the prism coupling method, using a Metricon Model 2010 at 543, 632.8 and 1553.2 nm. The instrument has an accuracy of ± 0.0001.

X-(9.478 GHz) and Q-band (34 GHz) continuous-wave electron paramagnetic resonance (CW-EPR) spectra were recorded at room temperature, on a Bruker Elexsys E580 spectrometer. HYSCORE experiments [31] were performed on a Bruker Elexys E580 spectrometer. X-band HYSCORE experiments were performed with the pulse sequence $\pi/2 - \tau - \pi/2 - T_1 - \pi - T_2 - \pi/2 - \tau$ – echo, with $t_{\pi/2}$ and t_π pulse lengths of 16 ns. Both time intervals T_1 and T_2 were incremented in 16 ns from the starting value of 96 ns. Q-band HYSCORE experiments were implemented using the remote detection technique [32] to avoid blind spot effects. The remote-echo detector sequence $\pi/2 - t_r - \pi/2 - \tau_r - \pi - \tau_r$ – echo was added at the end of the HYSCORE sequence, with $t_{\pi/2} = 16$ ns, $\tau_r = 200$ ns, and $t_r = 3$ μs. The fixed interpulse delay $\tau = 24$ ns was used in the HYSCORE sequence, while time intervals T_1 and T_2 were incremented in steps of 8 ns from the starting value 120 ns. Spectra were recorded at 20 K. Numerical simulation of the CW-EPR spectra was performed using the function “pepper” of the software package EasySpin [33] while HYSCORE simulations were performed using the function *saffron* from the EasySpin package.

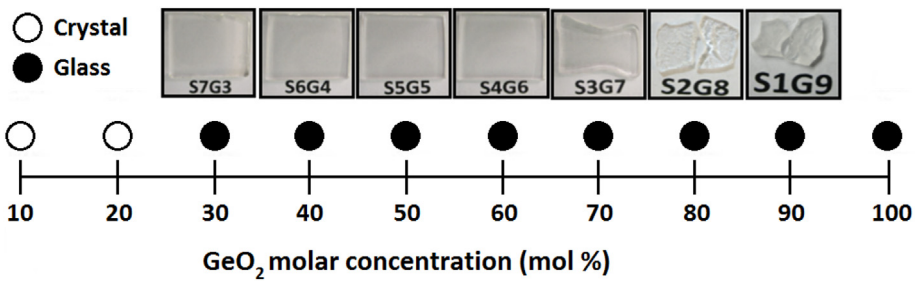

Fig. 1. Vitreous domain of the $SbPO_4$-GeO_2 glass system. Above each concentration is shown the photography of the correspondent glass.

Table 1
Chemical compositions, characteristic temperatures and the stability parameters for the binary glasses.

Samples	Glass composition (mol %)		Characteristic temperatures (°C)			ΔT (°C)
	$SbPO_4$	GeO_2	T_g	T_x	T_p	
S7G3	70	30	405	459	465	54
S6G4	60	40	404	500	506	96
S5G5	50	50	405	556	572	151
S4G6	40	60	412	617	658	205
S3G7	30	70	404	630	757	226
S2G8	20	80	404	663	722	259
S1G9	10	90	403	> 800	> 800	> 397

3. Results and discussion

The limits for glass formation were investigated in the binary system: (*100-x*)$SbPO_4$-*x*GeO_2. Fig. 1 shows the vitreous domain where samples containing > 30 mol% of GeO_2 form glasses, which is related with the fact that $SbPO_4$ is not itself a glass former, does not form long chains like those found in polyphosphate-based glasses [34]. All samples were optically homogeneous to naked eyes, colorless and free of strains. In Fig. 1 we represent the hypothetic composition of 100 mol% of GeO_2 as a glass, however, such sample was not obtained in this work due to experimental limitations, once it is well known that the GeO_2 is a common glass former with melting temperature higher than 1200 °C [35].

3.1. Differential scanning calorimetry (DSC)

For better readability, the samples were labeled as showed in Table 1. Chemical compositions, characteristic temperatures and values of the thermal stability parameter, $\Delta T = (T_x\text{-}T_g)$, for all glass samples, are summarized in Table 1.

Fig. 2a exhibit the thermal behavior of the glass samples as a function of chemical composition. The first interesting result is, regardless GeO_2 content, that T_g values remain constant, with exception of the S4G6 sample which shows a small increase of glass transition temperature. This fact suggests the incorporation of GeO_4 tetrahedral units into phosphate chains does not change the overall arrangement of the glass structure and only the substitution of PO_4 and SbO_4 units are expected. Moreover, GeO_2 incorporation clearly improves the thermal stability against devitrification ($\Delta T = T_x\text{-}\ T_g$) since the crystallization peak is shifted to higher temperatures. It is worth to note that S7G3 sample presents a narrow peak of crystallization indicating the presence of an unstable phase at low temperature. On the other hand, the increase of GeO_2 concentration makes the crystallization peak broader and this behavior are directly related to its slow crystallization kinetics.

However, while T_g seems not be affected by GeO_2 content, increasing its content, the crystallization peak shifts to higher temperatures and ΔT reaches values higher than 397 °C (sample S1G9). Fig. 2b shows the behavior of the glass transition temperature and thermal stability parameter as a function of the GeO_2 content. Such high ΔT is very important for preform production, used as a template to drawn optical fibers, or even to produce photonic crystal fibers [14].

3.2. Raman scattering

Raman spectra for all glass samples and reference compounds are shown in Fig. 3. The Raman spectrum of crystalline α-quartz GeO_2 is also presented (inset), mainly composed of GeO_4 tetrahedral units. We can notice that, between 800 and 1000 cm^{-1}, there are three bands which have been assigned to stretching vibration of Ge-O-Ge (856 cm^{-1}), O—Ge (880 cm^{-1}) and O-Ge-O (971 cm^{-1}) units. In the middle range energies of the spectrum, between 300 and 700 cm^{-1},

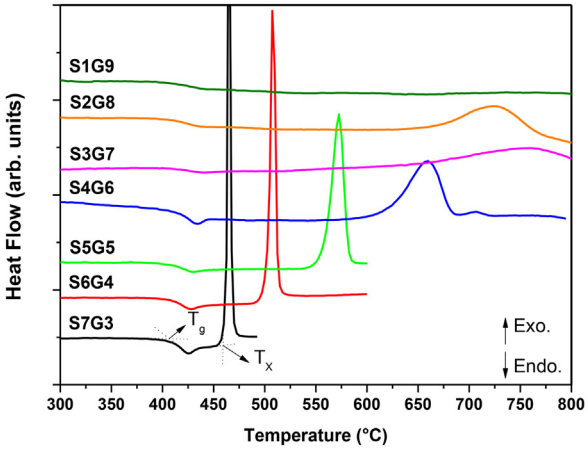

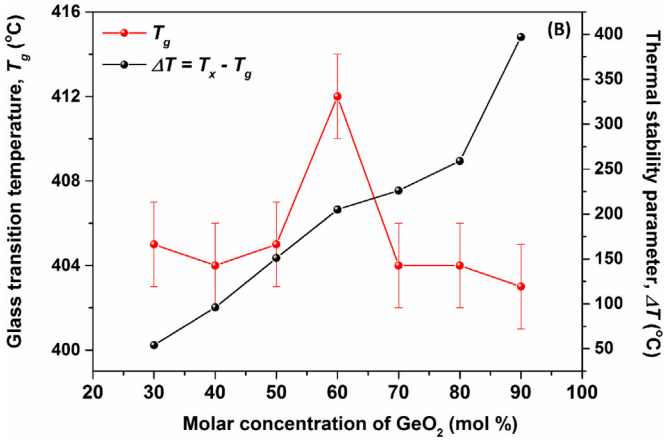

Fig. 2. (A) DSC curves of glass samples and (B) glass transition temperature (red dots) and thermal stability parameter (black dots) as a function of the GeO_2 content for samples in the binary system $SbPO_4$-GeO_2. (For interpretation of the references to colour in this figure legend, the reader is referred to the web version of this article.)

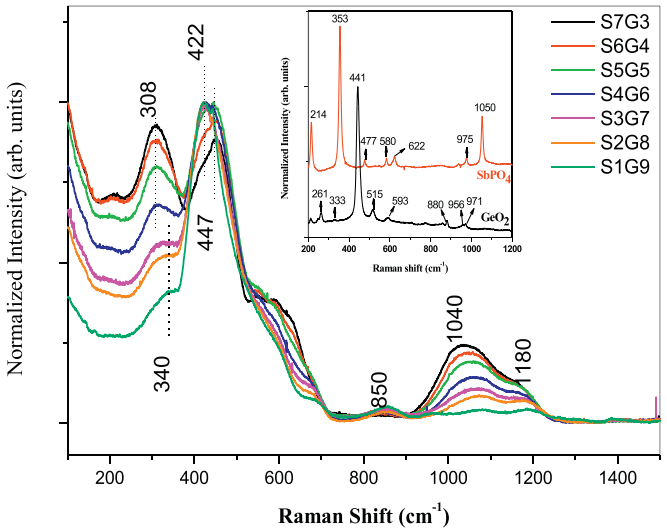

Fig. 3. Raman spectra of crystalline reference compounds and glass samples in the $SbPO_4$-GeO_2 system. The inset shows the spectra for both crystalline compounds used in the glass preparation.

there are four main bands assigned to bending mode vibrations of O-Ge-O bridges (333 cm^{-1}) and bending mode vibrations of Ge-O-Ge (441, 515, 593 cm^{-1}) [36].

It is well known that crystalline antimony orthophosphate ($SbPO_4$) has several spectral components in Raman between 100 and 1300 cm^{-1} as described early [12]. Three of them at highest energy region can be attributed to the asymmetric (1051 and 975 cm^{-1}) and symmetric stretching (934 cm^{-1}) modes of PO_4 tetrahedral units. At middle energy range (622, 580 cm^{-1}), vibrations are assigned to asymmetric bending modes of PO_4 while the band around 477 cm^{-1} was attributed to an asymmetric bending mode. The most part of these modes is probably coupled with Sb-O-P stretching modes. At low energy, the vibration around 540 cm^{-1} corresponds to a symmetric bending mode of the SbO_4E groups (E denotes a non-bonding electron pair) while lowest energies vibration (351 and 214 cm^{-1}) were assigned to groups modes.

The Raman spectra displayed in Fig. 3 show that the short-range structures of glasses frequently resemble those of corresponding crystals, although the fine features of crystal spectra are lost in glass spectra. Raman spectra of glass samples exhibit several features which can be used to monitor the structural dependence as a function of the composition. Low $SbPO_4$ content samples present very broad and faint bands at high energy region (~1040, ~1180 cm^{-1}), which are, respectively, attributed to both asymmetric and symmetric stretching of O-P-O bridges associated to Q^0 tetrahedral units linked by the oxygens in SbO_4 and GeO_4 units [37]. At 850 cm^{-1} a weak intensity band is observed for glasses containing > 50 mol% of GeO_2, which is attributed to Ge-O-Ge asymmetric stretching [37] of GeO_4 units or assigned to symmetric stretching motions of $Ge—O^-$ involving one non-bridging oxygen [38].

The frequency range, from 500 and 700 cm^{-1} envelops both GeO_4 (i.e. bending mode of Ge—O—Ge at 590 cm^{-1}), PO_4 and SbO_4 (i.e. symmetric bending of SbO_4units at 546 cm^{-1} and that assigned to PO_4 at 624 cm^{-1}) tetrahedral units and these bands progressively decrease as the GeO_2 content rises. It suggests the bands in this region are more related to PO_4 groups. To better understand the glass structural changes, deconvolutions of the broad bands located between 200 and 725 cm^{-1} were done for samples S7G3 and S1G9 (using Gaussians functions) as presented in Fig. 4. It is necessary to point out that the bands coming from both GeO_2 and $SbPO_4$ are overlapped in the region making difficult very precise assignments. Both spectra present six bands. Sample S7G3, show bands at 624 cm^{-1} (δ PO_4), 582 cm^{-1} (δ Ge-O-Ge and δ PO_4), 549 cm^{-1} (δ Ge-O-Ge) [12,39–40] The two bands around 404 and 456 cm^{-1} are clearly connected with Ge-O-Ge and SbO_4 modes. However, glassy GeO_2 also present one band very similar

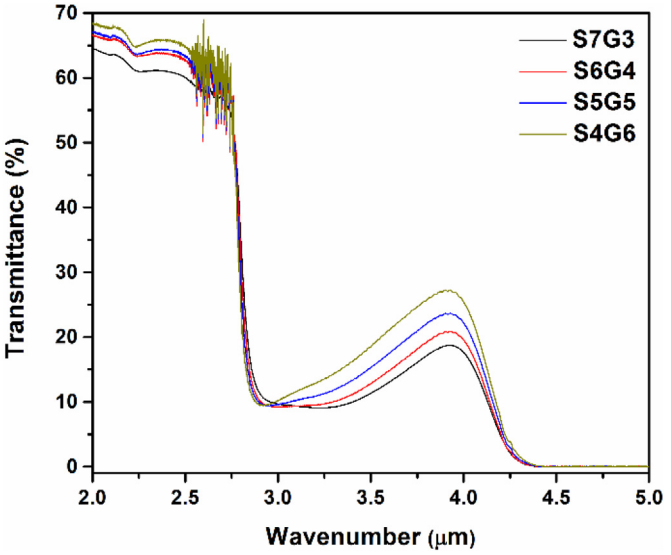

Fig. 5. Near-infrared transmittance spectra of glass samples in the binary system $SbPO_4$-GeO_2.

at 480 cm^{-1} [39]. Finally, the lower energy band also may encompass components from PO_4 and GeO_4 tetrahedral sites.

In this sense, a clearly structural change in function of GeO_2 content was observed by thermal analysis and Raman spectroscopy. The band around 413 cm^{-1} assigned to Ge-O-Ge symmetric stretching increases in intensity when $SbPO_4$ content decrease. It suggests that six-member rings of GeO_4 units exist since low GeO_2 concentration, while PO_4 and SbO_4 units appear linking the rings.

3.3. Infrared transmittance

Infrared transmittance spectra of glass samples are shown in Fig. 5. The multiphonon cut-off occurs at 2.7 μm and it is limited by the strong absorption band centered at 3 μm assigned to OH absorption and is comparable to other phosphate glasses [41]. Such large OH absorption can be reduced by producing the glass samples into a water-free atmosphere in a glove-box or using desiccant agents during the melting process. The reduction of OH content in the glass matrix will probably push the infrared cut-off to higher wavenumber up to ~4 μm, which is typical for germanate based glasses [42]. Moreover, the increase in transmittance at 3.9 μm is related to the increase of GeO_2 content.

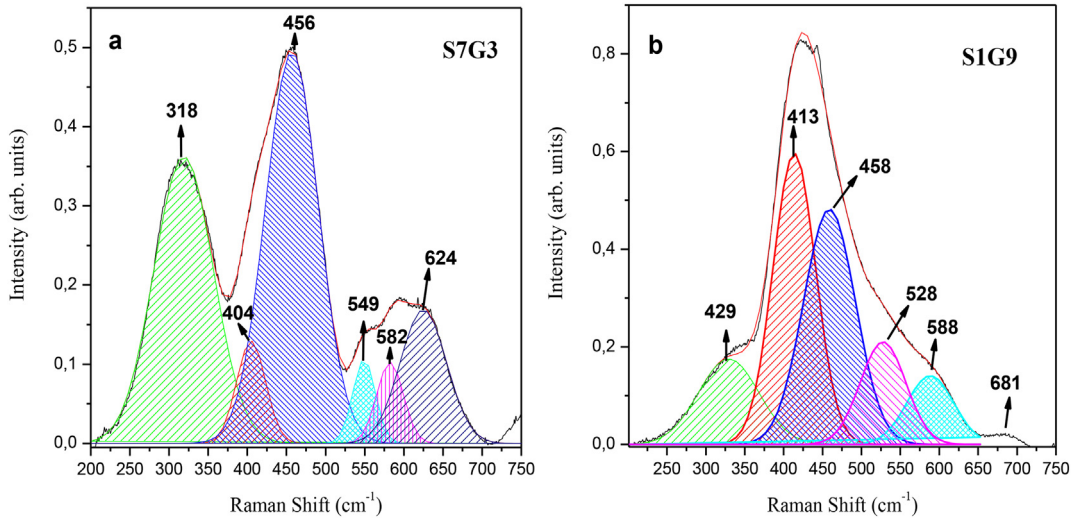

Fig. 4. Deconvolution bands for higher (a) and lower (b) $SBPO_4$ content samples.

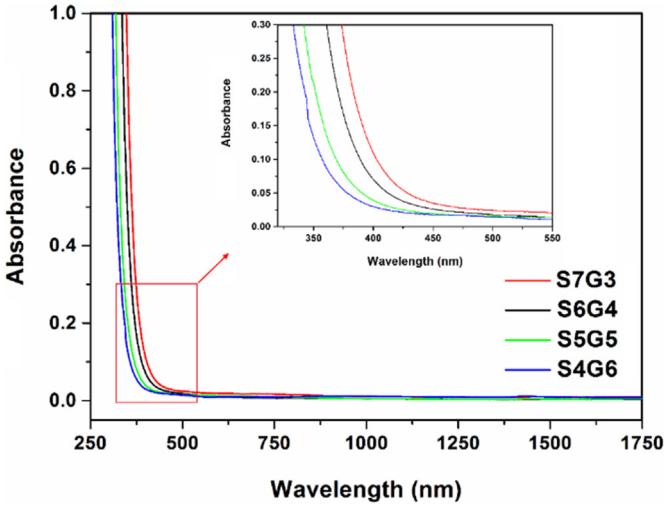

Fig. 6. UV–Visible-NIR absorption spectra of $SbPO_4$-GeO_2 glass samples.

3.4. UV–Vis-NIR absorption

The absorption spectra of the polished bulk glass samples from UV to NIR ranges are shown in Fig. 6. The inset shows the absorption edges shift to higher energy wavelengths as a function of the GeO_2 content. Considering the absorption band an electronic transition from the conduction to valence bands, the shift means that GeO_2 incorporation progressively increases the bandgap energy between these bands. This behavior is in agreement with the aforementioned structural discussion, where the glass network connectivity does not suffer substantial structural changes even at high GeO_2 concentration, which is also consistent with the increase of band gap energy. It was impossible to obtain the spectra for S3G7, S2G8, and S1G9 glass samples because they have highly viscous melts to be cast into the mold since the furnace temperature was limited to 1200 °C.

3.5. Linear refractive index

Linear refractive index values, n_o, were measured by using the prism couple technique, for compositions S7G3, S6G4, S6G5, and S4G6. The results identified a decrease of n_o values with GeO_2 content, ranging from 1.79 to 1.71 at 543 nm, 1.78 to 1.70 at 633 nm and from 1.75 to 1.67 at 1550 nm as shown in Fig. 7. This behavior can be explained thanks to the lower polarizability of germanium atoms compared to antimony. The decrease of antimony content contributes more efficiently to decrease refractive index due to the higher polarizability of Sb atoms.

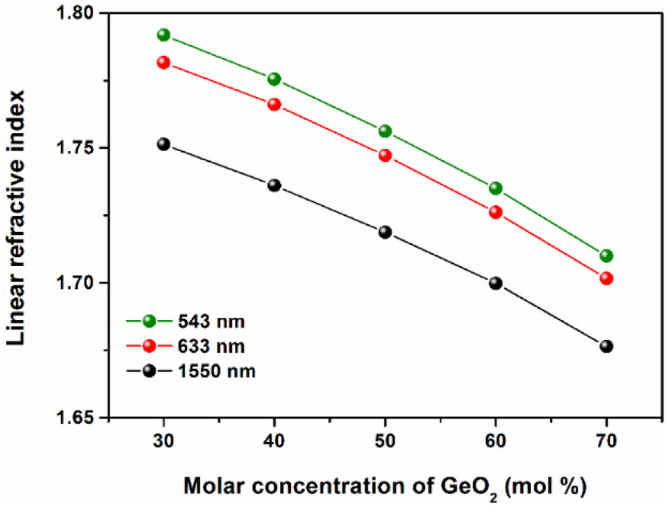

Fig. 7. Refractive index values as a function of GeO_2 molar concentration.

3.6. EPR measurements

Fig. 8 shows the X-band (left) and Q-band (right) EPR spectra measured at room temperature of theS4G6 glass doped with 0.1 mol% V_2O_5. Fig. 8(a), 8(b), 8(c) and 8(d) show the spectra of as-prepared glass and the same sample treated at 440 °C, 470 °C, and 500 °C, respectively. The EPR spectra are well resolved and indicate the presence of the paramagnetic V^{4+} ion. The V^{4+} ion has a 3d [1] electronic configuration, ground state [2]$D_{3/2}$ and spin $S = ½$. Vanadium has two stable isotopes with non- zero nuclear spin [50],V ($I = 6$) and [51]V ($I = 7/2$) with natural abundances 0.24% and 99.76%, respectively. Therefore, the isotropic EPR spectrum of isolated V^{4+} species is expected to show a hyperfine structure composed of eight lines, resulting from the dipole-dipole interaction between the magnetic moment of the [51]V nuclei and the electronic moment of the paramagnetic V^{4+} ion. The EPR spectra observed in the S4G6 glasses (Fig. 8a) shows overlap between different lines because of the presence of both, *g*-tensor anisotropy and the hyperfine coupling *A*-tensor anisotropy. The EPR spectra in Fig. 8 are similar to those reported for vanadium-doped glasses [19,24,43] and are typical of VO^{2+} ions in axially distorted sites. The EPR spectra can be described in terms of the spin-Hamiltonian for d [1] ions in axial symmetry,

$$H = g_{//}\beta H_Z S_z + g_{\perp}\beta(H_x S_x + H_y S_y) + A_{//} I_z S_z + A_{\perp}(I_x S_x + I_y S_y) \quad (1)$$

where β is the Bohr magneton, $g_{||}$and $g_{\perp}$ are the parallel and perpendicular components of the anisotropic g tensor, $A_{||}$ and $A_{\perp}$are the parallel and perpendicular hyperfine components of the hyperfine tensor *A*, and the other symbols have their usual meaning [21,43]. The first two terms in the Hamiltonian represent the interaction of the $S = ½$ electron spin with the external magnetic field *H,* i.e., the electron Zeeman interaction. The last two terms stand for the hyperfine interaction describing the interaction between the $S = ½$ electron spin with $I = 7/2$ nuclear spin of the [51]V isotope.

Because of the complex experimental EPR spectra in Fig. 8, the spin Hamiltonian parameters can only be obtained from a simulation of the EPR spectra in both X- and Q-band. The numerical simulations of the axial spin Hamiltonian (Eq. 1), showed in Fig. 8 (red lines), were obtained using the EasySpin package [33] in Matlab environment. The fits to the experimental EPR spectra of the S4G6 as-prepared glass and those treated at 440 °C were obtained assuming one VO^{2+} species with axial symmetry. For the glasses treated at 470 °C and 500 °C the experimental EPR spectra were satisfactorily simulated assuming two VO^{2+} sites with rhombic symmetry ($g_{xx} \neq g_{yy} \neq g_{zz}$, $A_{xx} \neq A_{yy} \neq A_{zz}$) and the simulated spectra were obtained by adding the contribution from components 1 and 2 with the Hamiltonian parameters given in Table 2.

Empirical models correlates the EPR isotropic *g*- and *A*-factors (g_{iso} and A_{iso}) to the type of functional vanadium centers of solid state systems, are used to establish the formation of V^{4+} or VO^{2+} in the material [43]. The values obtained for the S4G6 glass (sample A in Table 2),$g_{iso} = (g_{||} + 2g_{\perp})/3 = 1.9595$ and $A_{iso} = (A_{||} + 2A_{\perp})/3 = 318.3$ MHz (i.e., $106 \times 10^{-4}\,cm^{-1}$) are consistent with vanadium paramagnetic center of vanadyl form, VO^{2+}.

Further information regarding the coordination environment of VO^{2+} centers in the S4G6 glasses can be obtained from the analysis of the EPR spin Hamiltonian parameters. An octahedral site for the VO^{2+} ions can be excluded since the values of the principal components of the *g* tensor and the hyperfine coupling tensor do not satisfy the condition $g_{//} > g_{\perp}$ and $A_{//} > A_{\perp}$. The fact that $g_{//} < g_{\perp} < g_e$, where $g_e = 2.0023$ is the free electron *g*-value, and $A_{//} > A_{\perp}$ (Table 2) suggests that the paramagnetic centers are located in axially distorted octahedral sites

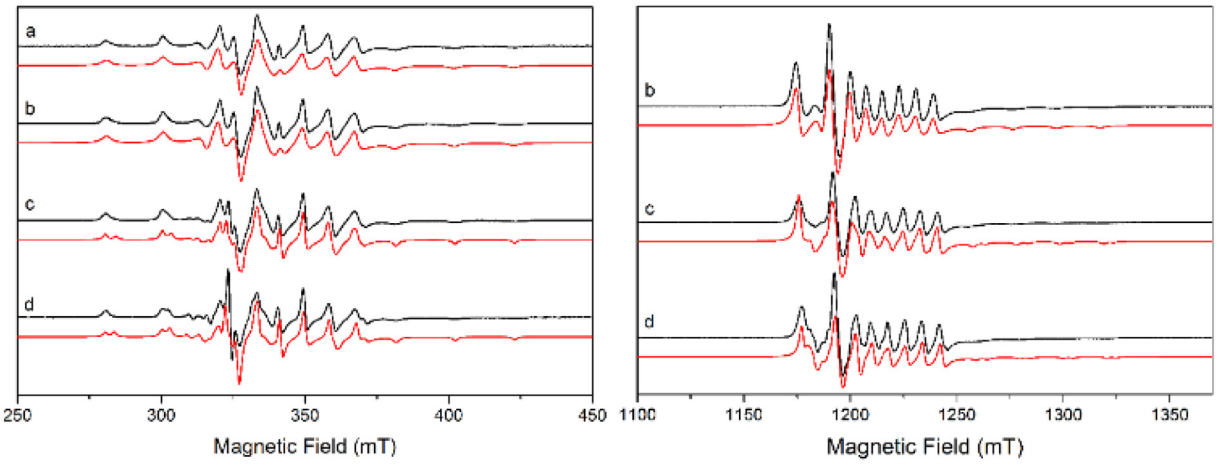

Fig. 8. X- (left) and Q-Band (right) continuous wave EPR spectra (black lines) and its numerical simulation (red lines) of samples without thermal treatment (a) and with thermal treatment at 440 °C (b), 470 °C (c), and 500 °C (d). (For interpretation of the references to colour in this figure legend, the reader is referred to the web version of this article.)

[44,45]. These relationships of $g_{||}$, $g_{\perp}$, $A_{||}$ and $A_{\perp}$values holds for many phosphate and borate glasses doped with vanadium reported in the literature and are ascribed to vanadyl ions in the octahedral site with a tetragonal compression [23,43].

From the values of the spin Hamiltonian parameters the value of dipolar hyperfine coupling parameter, *P*, and the Fermi contact interaction term, *K*, can be calculated by using the expression developed by Kivelson and Lee [23,43,45,46].

$$A_{II} = P\left[-\frac{4}{7} - K + \Delta g_{II} + \frac{3}{7}\Delta g_{\perp}\right] \quad (2)$$

$$A_{\perp} = P\left[\frac{2}{7} - K + \frac{11}{147}\Delta g_{\perp}\right] \quad (3)$$

The dipolar hyperfine coupling parameter is a measure of the radial distribution of the unpaired electron wave function. The Fermi contact interaction term is the dimensionless core polarization parameter represents the amount of unpaired electron density at the vanadium nucleus. The values of *P* and *K* for the $SbPO_4$ – GeO_2 glasses are given in Table 3. The values of the ratio ($\Delta g_{//}/\Delta g_{\perp}$) for the $SbPO_4$ – GeO_2 glasses, where $\Delta g_{//} = (g_{||} - g_e)$ and $\Delta g_{\perp} = (g_{\perp} - g_e)$, are also included in Table 3. This ratio is a measure of the degree of tetragonal distortion of the VO^{2+} sites [47,48]. It should be noted that the magnitude of the Fermi-contact interaction can also be used to estimate the tetragonality of the VO^{2+} site [27]. For samples C and D, we used $g_{\perp} = (g_{xx} + g_{yy})/2$ and $A_{\perp} = (A_{xx} + A_{yy})/2$.

The values of the ratio ($\Delta g_{//}/\Delta g_{\perp}$) and the parameters *P* and *K* of the $SbPO_4$ – GeO_2 glass are consistent with those reported for others phosphate glasses [27,49–50]. An interesting fact is that the values these parameters for the $SbPO_4$ – GeO_2 non-treated glass and those of the treated glass at 440 °C are similar to those found for the component 1 of the glasses treated at 470 °C and 500 °C (Table 3). Therefore, thermal treatment of the $SbPO_4$ – GeO_2 glass at temperatures between the glass transition (T_g~412 °C) and the onset of crystallization temperature (T_x~617 °C) does not alter the spin Hamiltonian parameters of component 1. This observation suggests that the coordination environment of VO^{2+}centers in the S4G6 glass does not change with the thermal treatment up to 500 °C. Nevertheless, for the glasses treated at 470 °C and 500 °C, a second VO^{2+} signal appears (component 2 in Tables 2 and 3) and their values of ($\Delta g_{//}/\Delta g_{\perp}$) and the Fermi constant term K is significantly higher, suggesting that the vanadyl ions of component 2 are in more tetragonally distorted octahedral sites than those in component 1. These results suggest that the coordination environment of VO^{2+}center in component 1 is different from those in component 2. Grunin et al. also observed a second V^{4+} signal in lithium aluminosilicate glasses during the first stage of glass crystallization. From the reported spin Hamiltonian parameters, the values of ($\Delta g_{//}/\Delta g_{\perp}$) and *K* can be derived for both, the V^{4+} spectrum in the glass and the second component. The results suggest that, in their system, the

Table 3
The dipolar hyperfine coupling parameter P, the Fermi contact interaction parameter K, and the value of ($\Delta g||/\Delta g\perp$) for the S4G6 glasses doped with 0.1 mol%V2O5. Non-treated glass (sample A) and glass treated at 440 °C, 470 °C, and 500 °C (samples B, C, and D, respectively). For samples C and D, we used $g\perp = (gxx + gyy)/2$ and $A\perp = (Axx + Ayy)/2$.

Sample	Comp.	$\left(\frac{\Delta g_{II}}{\Delta g_{\perp}}\right)$	P ($\times 10^{-4}$ cm^{-1})	K
A	–	3.1 ± 0.1	120.3 ± 0.3	0.85 ± 0.01
B	–	3.1 ± 0.1	119.7 ± 0.3	0.86 ± 0.01
C	1	3.1 ± 0.1	121.5 ± 0.3	0.85 ± 0.01
	2	4.1 ± 0.1	108.0 ± 0.3	0.97 ± 0.01
D	1	3.1 ± 0.1	119.0 ± 0.3	0.88 ± 0.01
	2	4.0 ± 0.1	111.0 ± 0.3	0.96 ± 0.01

Table 2
Summary of the spin Hamiltonian parameters obtained from the simulation of the experimental EPR spectra of the S4G6 glasses doped with 0.1 mol% of V2O5. As-prepared glass (sample A) and glass treated at 440 °C, 470 °C, and 500 °C (samples B, C, and D, respectively). The accuracy of the EPR parameters was estimated to be ± 0.0003 for g values and ± 2 MHz for hyperfine splitting constants.

Sample	g_{xx}	g_{yy}	g_{zz}	A_{xx}(MHz)	A_{yy}(MHz)	A_{zz} (MHz)	Area (%)
A	1.9770	1.9770	1.9245	205	205	545	100
B	1.9771	1.9771	1.9243	208	208	545	100
C Site 1	1.9740	1.9798	1.9249	195	218	548	66.14
Site 2	1.9854	1.9766	1.9154	236	207	532	33.86
D Site 1	1.9764	1.9784	1.9247	208	218	548	50.00
Site 2	1.9831	1.9762	1.9157	243	204	543	50.00

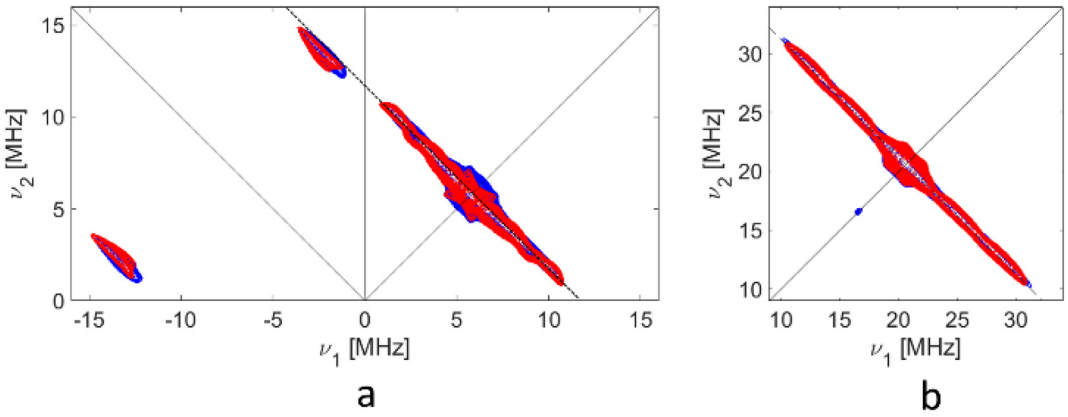

Fig. 9. HYSCORE spectra obtained at 20 K for the sample $SbPO_4$–GeO_2 treated at 500 °C (blue contours) and its numerical simulations (red contours). (a) X-Band at field position 333.7 mT. (b) Q-Band at field position 1196.0 mT. The antidiagonal line ($\nu_1 = -\nu_2 + 2\nu_P$) marks the position of features originated by the hyperfine interaction between the vanadium electron spin and the [31]P nuclear spin. (For interpretation of the references to colour in this figure legend, the reader is referred to the web version of this article.)

octahedral symmetry around V^{4+} ion is improved in the second EPR signal [28].

In order to clarify the local environment of V^{4+} ions in the glass matrix, we performed two-dimensional (2D) HYSCORE experiments. Fig. 9 shows typical HYSCORE spectra (blue contours) recorded at X- and Q-band frequencies of the S4G6 glass doped with 0.1 mol% V_2O_5 and thermally annealed at 500 °C. Orientationally selective experiments were carried out at both frequencies, at different magnetic field settings. The X-band HYSCORE spectrum features a ridge-shaped signal with maximum extension of approximately 10 MHz, centered at $\nu_P$in the (+,+) quadrant and a pair of cross peaks in the (−,+) quadrant centered at ≈8 MHz and separated by $2\nu_P$.These results clearly indicate the presence of directly coordinated phosphate groups, however, since the hyperfine couplings span the so-called cancellation condition ($A = 2\nu_I$) with spectral features appearing across the two quadrants, a better resolution is obtained by performing experiments at Q-band frequency (34 GHz) [51,31]. Under these circumstances the nuclear Zeeman interaction dominates ($A < 2\nu_I$) and an extended ridge, with maximum extension of approximately 20 MHz, centered at ν_P is observed, in the (+,+) quadrant. In order to avoid blind spot effects the remote detection technique was used and, since only part of the correlation pattern is observed due to the limited excitation bandwidth, experiments at different magnetic field settings were performed [32]. Inspection of Fig. 9b, shows that the correlation ridge lies on the $\nu_1 = -\nu_2 + 2\nu_P$ antidiagonal and shows negligible orientation dependence, indicating that the hyperfine coupling is dominated by the isotropic Fermi contact term. Under these circumstances, the ridge shape of the signal results from a distribution of a_{iso} values and does not arise from dipolar interactions. This analysis is corroborated by computer simulations, from which, a distribution of a_{iso} values ranging from 2 MHz to 15 MHz and a maximum dipolar coupling in the order of $T = 3 \pm 1$ MHz is obtained.

The isotropic couplings obtained from the experiments are induced by spin density transfer to [31]P ions through the directly coordinated oxygen anions and are particularly sensitive to structural variations, the values depending markedly on *V*-O-P bond angles and lengths [31]. The spin population in the phosphorous 3 s orbital can be estimated in the range |0.02–0.15|%, by:

$$\rho_{P(3s)} = \frac{a_{iso}}{a_0}\frac{g_e}{g_{iso}} \quad (4)$$

where a_0 = 10,201.44 MHz is the unit spin density of the phosphorous 3 s orbital [52] and $g_{iso} = (g_{xx} + g_{yy} + g_{zz})/3$. These values agree with results obtained for the incorporation of vanadyl ions in the framework of crystalline aluminophosphates [31]. In the case of a thermally annealed glass, one can expect a distribution of distances and angles in the V–O–P fragments, which explains the large distribution of a_{iso} values compared with the case of crystalline aluminophosphates [31].

4. Conclusions

A novel stable $SbPO_4$-GeO_2 binary glass system has been synthesized and thermal, structural and optical characterized. These glasses exhibit excellent thermal stability as well as low transition temperature associated with good mechanical resistance, low viscosity and high transparency in the infrared region. In addition, the change of these properties is intrinsically associated with GeO_2 incorporation, making the glass system an excellent candidate for optical fiber and planar waveguides production. Moreover, the addition of GeO_2 into the $SbPO_4$ network facilitate incorporation of rare-earth ions since antimony-based glasses are well known to have very low rare-earth solubility. EPR spectra of S4G6 glasses doped with V_2O_5, heat treated at different temperatures, ranging from the glass transition temperature to the onset of crystallization temperature, shows the characteristic eight-line hyperfine splitting spectrum. These spectra were described in terms of the spin-Hamiltonian for d [1] ions in axial symmetry. The spin Hamiltonian parameters obtained from the simulated spectra indicated that the paramagnetic tetravalent vanadium ions in the glasses exist as vanadyl form, VO^{2+}, located in axially distorted octahedral sites. For the glasses treated at higher temperatures, a second VO^{2+} component appears in the EPR spectra and the analysis of the spin-Hamiltonian parameters suggests that these vanadyl ions are in more tetragonally distorted octahedral sites than those in the glass. HYSCORE experiments were performed in the sample treated at 500 °C and show that the VO^{2+} ions are found near the phosphate groups in the glass. The V—P hyperfine interaction is dominated by the Fermi contact term (a_{iso}), arising from a trough bond spin transfer mechanism. A distribution of values ranging from 2 MHz to 15 MHz is observed corresponding to a maximum spin population in the [31]P 3 s orbital of about 0.15%. The distribution in a_{iso} values deduced from the HYSCORE experiments corresponds to a smooth distribution of V-O-P binding moieties, as expected in a glassy matrix.

Acknowledgment

The authors acknowledge grants number 2013/07793-6 from São Paulo Research Foundation – FAPESP, CNPq and CAPES (Brazilian agencies) for financial support. I. D. A. Silva acknowledges Prof. Mario Chiesa and Dr. Elena Morra for the hospitality at the University of Turin during a secondment supported by a USP-Santander fellowship (USP-

PRPG 04/2016).

References

[1] R.K. Brown, J. of Non-Cryst. Sol. 263–264 (2000) 1–28.
[2] E.L. Falcão-Filho, C.B. de Araújo, C.A.C. Bosco, G.S. Maciel, L.H. Acioli, M. Nalin, Y. Messaddeq, J. Appl. Phys. 97 (2005) 013505.
[3] V. Besse, A. Fortin, G. Boudebs, P.S. Valle, M. Nalin, C.B. de Araújo, App. Phys. B. 117 (2014) 891–895.
[4] D. Manzani, T. Gualberto, J.M.P. Almeida, M. Montesso, C.R. Mendonça, V.A.G. Rivera, L. de Boni, M. Nalin, S.J.L. Ribeiro, J. Non-Cryst. Sol. 443 (2016) 82–90.
[5] H. Takebe, T. Ishibashi, T. Murata, K. Morinaga, J. Cer. Soc. Jap. 11 (2003) 0168–0170.
[6] T.M. Monro, H. Ebendorff-Heidepriem, Annu. Rev. Mater. Res. 36 (2006) 467–495.
[7] K. Davis, K. Miura, N. Sugimoto, K. Hirao, Opt. Lett. 21 (1996) 1729.
[8] R. Osellame, N. Chiodo, G. Della Valle, G. Cerullo, R. Ramponi, P. Laporta, A. Kili, U. Morgner, O. Svelto, IEEE J. Sel. Top. Quant. Electr. 12 (2006) 277.
[9] G. Della Valle, S. Taccheco, R. Osellame, A. Festa, G. Cerullo, P. Laporta, Opt. Express 15 (2007) 3190.
[10] E.L. Falcão-Filho, C.A.C. Bosco, G.S. Maciel, C.B. Araujo, M. Nalin, Y. Messaddeq, Appl. Phys. Lett. vol. 83 (2003) 1292–1294.
[11] M. Nalin, M.I. Poulain, M.A. Poulain, S.J.L. Ribeiro, Y. Messaddeq, J. Non-Cryst. Sol. 284 (2001) 110–116.
[12] M. Nalin, Y. Messaddeq, S.J.L. Ribeiro, M. Poulain, V. Briois, G. Brunklaus, C. Rosenhahn, B.D. Mosel, H. Eckert, J. Mater. Chem. 4 (2004) 3398–3405.
[13] H. Takahashi, I. Sugimoto, J. Lightwave Technol. 2 (1984) 613–616.
[14] H.T. Munasinghe, A. Winterstein-Beckmann, C. Schiele, D. Manzani, L. Wondraczek, V. ShahraamAfshar, Tanya M. Monro, H. Ebendorff-Heidepriem, Opt. Mat. Express 3 (2013) 1488–1503.
[15] M. Pal, J. Mater. Res. 11 (1996) 1831–1835.
[16] S.R. Friberg, Y. Silberberg, M.K. Oliver, M.J. Andrejco, M.A. Saifi, Appl. Phys. Lett. 51 (1987) 1135–1137.
[17] G. Della Valle, R. Osellame, N. Chiodo, S. Taccheo, G., Cerullo and P, Laporta. Opt. Express 13 (2005) 5976–5982.
[18] J.R. Pilbrow, Clarendon Press, Oxford (1990).
[19] D.L. Griscom, J. Non-Cryst. Sol. 40 (1980) 211–272.
[20] P.J. Carl, S.L. Isley, S.C. Larsen, J. Phys. Chem. A 105 (2001) 4563–4573.
[21] O.R. Nascimento, C.J. Magon, J.F. Lima, J.P. Donoso, E. Benavente, J. Paez, V. Lavayen, M.A. Santa Ana, G. Gonzalez, J. Sol-Gel Sci. Technol. 45 (2008) 195–204.
[22] W. Low, Paramagnetic Resonance on Solids. In: Solid State Physics, supplement 2 Academic Press, 1960.
[23] J.S. Kumar, V. Madhuri, J.L. Kumari, S. Cole 44 (2013) 479–494.
[24] G.V. Honnavar, K.P. Ramesh, S.V. Bhat, J. Phys. Chem. A 118 (2014) 573–578.
[25] M. Rada, L. Rus, S. Rada, P. Pascuta, S. Stan, N. Dura, T. Rusu, E. Culea, J. Non-Cryst. Sol. 414 (2015) 59–65.
[26] R. Kripal, M. Bajpai, J. Alloys Compd. 490 (2010) 5–10.
[27] H. Hosono, H. Kawazoe, T. Kanazawa, J. Non-Cryst. Sol. 37 (1980) 427–432.
[28] V.S. Grunin, V.A. Ioffe, I.S. Yanchevskaya, Z.N. Zonn, J. Non-Cryst. Sol. 13 (1973/74) 243–250.
[29] S. Gupta, N. Khanijo, A. Mansingh, J. Non-Cryst. Sol. 181 (1995) 58–63.
[30] Y. Li, K. Liang, J. Cao, B. Xu, J. Non-Cryst. Sol. 356 (2010) 502–508.
[31] A. Pöppl, L. Kevan, J. Phys. Chem. 100 (1996) 3387–3394.
[32] S. Maurelli, G. Berlier, M. Chiesa, F. Musso, F. Corà, J. Phys. Chem. C 118 (2014) 19879–19888.
[33] H. Cho, S. Pfenninger, C. Gemperle, A. Schweiger, R.R. Ernst, Chem. Phys. Lett. 160 (1989) 391–395.
[34] S. Stoll, A. Schweiger, J. Magn. Reson. 178 (2006) 42–55.
[35] D. Manzani, C.B. de Araújo, G. Boudebs, Y. Messaddeq, S.J.L. Ribeiro, J. Phys. Chem. B 117 (2013) 408–414.
[36] A. Varshneya, Fundamentals of Inorganic Glasses, 1st Edition, Academic Press, 1993.
[37] R. Kaindl, D.M. Tobbens, S. Penner, T. Bielz, S. Soisuwan, B. Klotzer, Phys. Chem. Miner. 38 (2012) 47–55.
[38] G.S. Henderson, R.T. Amos, J. of Non-Cryst. Sol. 328 (2003) 1–19.
[39] D. Di Martino, L.F. Santos, A.C. Marques, R.M. Almeida, J. of Non-Cryst. Sol. 293 (2001) 394–401.
[40] C. Maurel, T. Cardinal, P. Vinatier, L. Petit, K. Richardson, N. Carlie, F. Guillen, M. Lahaye, M. Couzi, F. Adamietz, V. Rodriguez, F. Lagugné-Labarthet, V. Nazabal, A. Royon, L. Canioni, Mater. Res. Bull. 43 (2008) 1179–1187.
[41] E.I. Kamitsos, Y.D. Yiannopoulos, M.A. Karakassides, G.D. Chryssikos, H. Jain, J. Phys. Chem. 100 (1996) 11755–11765.
[42] D. Manzani, R.G. Fernandes, Y. Messaddeq, S.J.L. Ribeiro, F.C. Cassanjes, G. Poirier, Opt. Mater. 33 (2011) 1862–1866.
[43] K. Han, D. Kim, D. Kim, K.C. Choi, Sci. Rep. 6 (2016) 31207.
[44] A. Agarwal, S. Khasa, V.P. Seth, M. Arora, J. Alloys Compd. 568 (2013) 112–117.
[45] P. Jakes, R.A. Eichel, Mol. Phys. 110 (2012) 277–282.
[46] A. Davidson, M. Che. J. Phys. Chem. 96 (1992) 9909–9915.
[47] D. Kivelson, S.K. Lee, J. Chem. Phys. 41 (1964) 1896–1903.
[48] H. Farah, J. Alloys Compd. 453 (2008) 288–291.
[49] D. Prakash, V.P. Seth, I. Chand, P. Chand, J. Non-Cryst. Sol. 204 (1996) 46–52.
[50] C.I. Andronache, Mater. Chem. Phys. 136 (2012) 281–285.
[51] R.V.S.S.N. Ravikumar, V.R. Reddy, A.V. Chandrasekhar, B.J. Reddy, Y.P. Reddy, P.S. Rao, J. Alloys Compd. 337 (2002) 272–276.
[52] A. Schweiger, G. Jeschke, Principles of Pulse Electron Paramagnetic Resonance, Oxford University Press, New York, 2001.